

# The evolving slope of the stellar mass function at $0.6 \leq z < 4.5$ from deep WFC3 data

P. Santini<sup>1</sup>, A. Fontana<sup>1</sup>, A. Grazian<sup>1</sup>, S. Salimbeni<sup>2</sup>, F. Fontanot<sup>3</sup>, D. Paris<sup>1</sup>, K. Boutsia<sup>1</sup>, M. Castellano<sup>1</sup>, F. Fiore<sup>1</sup>, S. Gallozzi<sup>1</sup>, E. Giallongo<sup>1</sup>, A. M. Koekemoer<sup>4</sup>, N. Menci<sup>1</sup>, L. Pentericci<sup>1</sup>, and R. Somerville<sup>4,5</sup>

<sup>1</sup> INAF - Osservatorio Astronomico di Roma, via di Frascati 33, 00040 Monte Porzio Catone, Italy.

<sup>2</sup> Astronomy Department, University of Massachusetts, Amherst, MA 01003, U.S.A.

<sup>3</sup> INAF - Osservatorio Astronomico di Trieste, Via G.B. Tiepolo 11, 34131 Trieste, Italy.

<sup>4</sup> Space Telescope Science Institute, 3700 San Martin Drive, Baltimore, MD 21218.

<sup>5</sup> Department of Physics and Astronomy, Johns Hopkins University, Baltimore, MD 21218.

Received .... ; accepted ....

## ABSTRACT

We used Early Release Science observations taken with the Wide Field Camera 3 (WFC3) in the GOODS-S field to study the Galaxy Stellar Mass Function (GSMF) at  $0.6 \leq z < 4.5$ . Deep WFC3 near-IR data ( $Y$  down to 27.3,  $J$  and  $H$  down to 27.4 AB mag at  $5\sigma$ ), as well as the deep  $K_S$  (down to 25.5 at  $5\sigma$ ) Hawk-I band, provide an exquisite sample which makes possible an unprecedented determination of the low-mass-end of the GSMF, thanks to a deep (down to  $M_* \simeq 7.6 \cdot 10^9 M_\odot$  at  $z \sim 3$ ) and at the same time accurate probe of low mass galaxies. Although the area used is relatively small ( $\sim 33 \text{ arcmin}^2$ ), still we found general good agreement with previous works on the entire mass range. Our results show that the slope of the faint-end is increasing with redshift, from  $\alpha = -1.44 \pm 0.03$  at  $z \sim 0.8$  to  $\alpha = -1.86 \pm 0.16$  at  $z \sim 3$ , and indications exist that it does not steepen further from  $z \sim 3$  to  $z \sim 4$ . This result is robust against the degeneration of the  $M^*$  parameter. The steepness of the GSMF faint-end solves the well known discrepancy between the Stellar Mass Density (SMD) and the integrated star formation history at  $z > 2$ . However, we confirm the excess of integrated star formation history with respect to the SMD at  $z < 2$ , by a factor of  $\sim 2-3$ . The comparison of the observations with theoretical predictions shows that the models forecast a larger abundance of low mass galaxies, at least up to  $z \sim 3$ , as well as a dearth of massive galaxies at  $z \sim 4$  with respect to the data, and that the predicted SMD is generally overestimated at  $z \lesssim 2$ .

**Key words.** Galaxies: luminosity function, mass function - Galaxies: evolution - Galaxies: high-redshift - Galaxies: fundamental parameters

## 1. Introduction

Understanding the assembly of stellar mass in galaxies is a fundamental step towards a description of galaxy evolution. Key tools to study this process through cosmic time are the Galaxy Stellar Mass Function (GSMF) and its integral over masses (the Stellar Mass Density, SMD hereafter).

Therefore, it comes as no surprise that most extragalactic surveys in the last decade were used to determine the shape and evolution of the GSMF as a function of redshift. Earliest results based on small field surveys revealed that the stellar mass density decreases with increasing redshift, as expected in the framework of the currently accepted cosmological hierarchical scenario, both in terms of integrated SMD (e.g. Giallongo et al. 1998; Dickinson et al. 2003; Fontana et al. 2003; Rudnick et al. 2003) as well as of the detailed GSMF (e.g. Fontana et al. 2004; Drory et al. 2004, 2005). More recently, many indications were provided that the evolution of the GSMF occurs more rapidly for more massive galaxies than for low mass ones (e.g. Fontana et al. 2006; Pozzetti et al. 2007; Pérez-González et al. 2008; Kajisawa et al. 2009; Marchesini et al. 2009), a behaviour known as downsizing in stellar mass (see Fontanot et al. 2009, and references therein). The advent of near- and mid-infrared facilities, above all the Spitzer telescope, allowed to reduce the uncertainties in the stellar mass estimates and especially

to extend the analysis to  $z \gtrsim 3$  (e.g. Fontana et al. 2006; Kajisawa et al. 2009; Caputi et al. 2011). In parallel, wide field surveys provided large samples with more accurate statistics (Drory et al. 2009; Pozzetti et al. 2010; Bolzonella et al. 2010; Marchesini et al. 2010; Ilbert et al. 2010). One of the key results of these surveys was the demonstration that the shape of the GSMF cannot be described by a (widely adopted) single Schechter function at least up to  $z \simeq 1.5$ , showing departing features from this parametric form that result from the superposition of individual distributions for the red and blue galaxy population (Ilbert et al. 2010; Pozzetti et al. 2010; Bolzonella et al. 2010; Mortlock et al. 2011) or/and from a change with stellar mass in star formation efficiency or galaxy assembly rate (Drory et al. 2009).

An accurate knowledge of the GSMF is also a sensitive test for modern galaxy evolutionary models. Since the beginning, much interest on the GSMF was triggered by the possibility of constraining the physics of the evolution of more massive galaxies which, according to the hierarchical structure formation scenario, are the results of merging of lower mass objects at earlier time (Cole et al. 1994). In addition, in order to achieve a complete view of the galaxy formation picture, an important goal is a good knowledge of the properties of low mass galaxies at high redshift. The slope of the GSMF at small masses may also represent a critical benchmark for current galaxy formation models. There is growing evidence that the number of low mass galaxies in the Universe is systematically

Send offprint requests to: P. Santini, e-mail: paola.santini@oa-roma.inaf.it

overpredicted by most or all theoretical models (Fontana et al. 2006; Fontanot et al. 2009; Marchesini et al. 2009). A very similar evidence appears also in the analysis of the luminosity functions (Poli et al. 2001; Marchesini & van Dokkum 2007; Lo Faro et al. 2009; Henriques et al. 2011). A particularly striking aspect of the mismatch is that it appears in different renditions of theoretical models, suggesting that it marks some fundamental incompleteness in our theoretical understanding of galaxy formation and growth.

While a global picture is emerging from these investigations, many outstanding questions are still to be addressed. In general, the various GSMF presented in the literature agree reasonably well at  $z = 0 - 5$ , although disagreements exist, somewhat increasing at high redshift (Caputi et al. 2011; González et al. 2011; Marchesini et al. 2010; Mortlock et al. 2011), which are not explained only by field-to-field variance. At even higher redshift, the available estimates of the SMD are based on UV-selected samples, and hence potentially incomplete in mass, and/or are often derived by adopting average mass-to-light ratios for the whole population rather than a detailed object-by-object estimate (González et al. 2011). Finally, and particularly relevant for the main topic of this paper, the GSMF at small masses is highly uncertain at intermediate and high redshift, since current samples do not extend at the depths required to establish its slope with good accuracy. These uncertainties are due to a number of observational limitations.

Besides uncertainties connected with the GSMF computation, it must not be forgotten that the very estimates of stellar masses from broad band photometry are potentially affected by many systematic uncertainties, even when accurate redshifts are available. Part of this uncertainty is due to the lack of knowledge of important parameters of the stellar population, as metallicity or extinction curve. The modelling of highly uncertain phases of stellar evolution is another source of uncertainty: in particular the different treatment of the Thermally Pulsating Asymptotic Giant Branch (TP-AGB) phase is the source of the highest discrepancies in simple stellar population models (see e.g. Maraston 2005; Marigo et al. 2008), and it has relevant implications in the estimate of near-infrared luminosities and stellar masses for galaxies dominated by intermediate age stellar populations ( $\sim 1$  Gyr). The largest bias is due to the difficulties in reconstructing the star formation history of each galaxy, that is necessary to estimate the appropriate  $M_*/L$  ratio, and that may be poorly described by simplistic models like those adopted in the stellar synthesis codes (Maraston et al. 2010; Lee et al. 2010).

All these uncertainties contribute to one of the main puzzles that appear in present-day observational cosmology: the mismatch between the observed SMD and the integrated star formation rate density (SFRD) (e.g. Hopkins & Beacom 2006; Fardal et al. 2007; Wilkins et al. 2008). In principle, these two observables represent independent approaches to study the mass assembly history from different points of view. However, the integrated star formation history, after considering the gas recycle fraction into the interstellar medium, appears higher than the observed stellar mass density at all redshifts. Several authors brought to light a severe discrepancy (up to a factor of  $\sim 4$  at  $z \sim 3$ , Wilkins et al. 2008). Moreover, if the merging contribution to the stellar mass build-up is accounted for (Drory & Alvarez 2008), the agreement gets even worse. Intriguingly, the integrated SFRD exceeds the observed SMD, implying that we are either overestimating the SFRD, or missing a substantial part of massive galaxies, or underestimating their mass, or finally failing in reconstructing the low mass tail of the GSMF. An Initial Mass

Function (IMF) varying over cosmic time was invoked to reconcile the two observables (Fardal et al. 2007; Wilkins et al. 2008). However, before invoking the non-universality of the IMF, it must be noted that both the SFRD and the SMD are affected by large uncertainties. The measure of the star formation rate is itself particularly difficult, either highly dependent on uncertain dust corrections (e.g. Santini et al. 2009; Nordon et al. 2010) or limited to the brightest far-infrared galaxies at  $z < 2 - 3$  (Rodighiero et al. 2010). On the stellar mass density side, besides uncertainties connected with the stellar mass estimate itself, a major role is played by the poor knowledge of the low mass tail of the GSMF. Due to limited depth of current IR surveys, the estimate of the faint-end slope basically relies on large extrapolations. A wrong estimate, given the large number density of low mass objects, could translate into non-negligible errors on the stellar mass density.

A robust estimate of the slope of the GSMF is necessary to provide better constraints on all these aspects. In this work we take advantage of the recent deep near-IR observations carried out by WFC3@HST in the upper part of the GOODS-S field in the  $Y$ ,  $J$  and  $H$  bands and by Hawk-I@VLT in the  $K_S$  band. These data allow accurate measurements of the stellar mass to very low limits. In this respect, we extend to higher redshifts and lower masses the deep analysis carried out by Kajisawa et al. (2009). The only study of comparable depth is the recent work of Mortlock et al. (2011), also based on WFC3 data. However, the greater depth of the Early Release Science (ERS) images used in this work and the conservative cuts that we apply to the sample ensure an excellent overall photometric quality, as we discuss in Sect. 3.3. Unfortunately, the area covered by ERS observations is small compared to recent surveys, and is slightly overdense. This feature somewhat limits the universal validity of our results regarding the SMD, especially in the intermediate redshift bins, although we have chosen our redshift intervals in order to keep the known clusters and groups (discussed in Sect. 2) mostly confined in two of them. However, we show that the study of the faint-end slope, which represents the main topic of the present analysis, is not significantly affected by these cosmic variance effects. In addition, this work represents an exercise to explore the possibilities of future deep WFC3 observations, such as those of the CANDELS survey (Grogin et al. 2011; Koekemoer et al. 2011), which will cover a much more extended area over various fields with depth comparable to the ERS observations.

The paper is organized as follows: after introducing the data in Sect. 2, we present the stellar mass estimate and the stellar mass function in Sect. 3, the analysis of the faint-end slope in Sect. 4, the stellar mass density and its comparison with the integrated SFRD in Sect. 5, and the comparison with theoretical predictions in Sect. 6. Sect. 7 summarizes our results. In the following, we adopt the  $\Lambda$ -CDM concordance cosmological model ( $H_0 = 70$  km/s/Mpc,  $\Omega_M = 0.3$  and  $\Omega_\Lambda = 0.7$ ). All magnitudes are in the AB system.

## 2. The data sample

This work exploits a new set of near-IR images which provide a significant improvement in photometric quality and depth over existing surveys. The first component is the public release of the Early Release Science (ERS) observations taken with Wide Field Camera 3 (WFC3), the new near-IR camera on board HST. ERS observations cover an area of  $\sim 50$  arcmin $^2$ , located in the northern  $\sim 30\%$  of the GOODS-South field. They were taken in three filters,  $Y_{098}$ ,  $J_{125}$  and  $H_{160}$ , which reach 27.3 ( $Y$ ) and 27.4 ( $J$ ,  $H$ ) magnitudes at  $5\sigma$  in an area of  $\sim 0.11$  arcsec $^2$ . We used the

ERS mosaics produced as described in Koekemoer et al. (2011); see also Grazian et al. (2011) for details on the catalogs, and Windhorst et al. (2011) for a full description of the ERS observational program.

We complemented these images with new deep  $K_S$  band images taken over the GOODS-S field with the near-IR VLT imager Hawk-I. The latter were taken in the framework of a program designed to search for  $z \sim 7$  galaxies (Castellano et al. 2010a,b). In the  $K_S$  band, the surveyed area covers 80% of the WFC3 ERS area. Because of that and after excluding uncertain image edges, the available area reduces to  $\sim 33$  arcmin $^2$ . Data reduction of the  $K_S$  images is analogous to the procedure used for others Hawk-I data (Castellano et al. 2010a). The net exposure time is 25200s, with a  $1\sigma$  r.m.s. of 1.26 counts per second in a 1" aperture. The magnitude limit at  $5\sigma$  is  $\sim 25.5$ , one magnitude deeper than the previous ISAAC  $K_S$  band.

We finally built a multiwavelength GOODS-ERS catalog adding the other public images available in the GOODS-S field. They include the ACS images in the  $BVIZ$  bands (Giavalisco et al. 2004), the deep  $UR$  images from VIMOS@VLT (Nonino et al. 2009) and the four IRAC bands at 3.6, 4.5, 5.8 and 8.0  $\mu\text{m}$ . With respect to the data set used to assemble our previous GOODS-MUSIC sample, (Grazian et al. 2006; Santini et al. 2009), the present GOODS-ERS data set benefits not only of the much deeper IR coverage provided by the new WFC3 and  $K_S$  band data, but also of a deeper version of the  $z$  band image (which nearly doubles the exposure time of the previous), of a deeper  $U$  band image and of a brand new  $R$  image. On this data set we extracted a 14 bands multiwavelength catalog using the  $H$  band as detection image. Colours were accurately obtained with the same technique used in the GOODS-MUSIC catalog, where we adopted the PSF-matching code CONVPHOT (De Santis et al. 2007) to accurately deblend objects in the ground-based and Spitzer images. We note that the depth of the  $H$  band even exceeds the depth of the bluest bands, resulting in very poor photometric information on the faintest  $H$ -selected objects.

The catalog was cross-correlated to existing spectroscopic samples. For sources lacking spectroscopic information, photometric redshifts were computed by fitting the 14 bands multiwavelength photometry to the PEGASE 2.0 templates (Fioc & Rocca-Volmerange 1997, see details in Grazian et al. 2006). The accuracy reached by the photometric redshifts is very high, the absolute scatter  $|\Delta z|/(1+z_{\text{spec}})$  being equal to 0.03, with only 3% of severe outliers ( $|\Delta z|/(1+z_{\text{spec}}) > 0.5$ ). The statistical error associated with each photometric redshift was used to evaluate the limiting magnitude at which a reliable mass function can be computed. We found that a limit  $H \simeq 26$  (or, equivalently,  $K_S \simeq 25.5$ ) is appropriate to keep the error on the mass estimate (see next section) within 0.3 dex and the relative scatter of photometric redshifts  $|\Delta z|/(1+z) < 0.1$  for 85% of objects, and we adopt this in the following. From the analysis of the individual photometric redshift probability distributions, we can compute the fraction of "reliable" candidates. We considered a candidate to safely lie within a given redshift interval when the integral of its probability distribution curve, normalized to unity, over that interval is larger than 90%. Moreover, we accepted a certain level of tolerance in the definition of the redshift range to allow for the uncertainty in photometric redshifts. Following this method, of all  $K_S < 25.5$  sources with  $z_{\text{phot}} > 2$ , a secondary redshift solution at  $z_{\text{phot}} < 1.5$  can be discarded in 97.2% of the sources. This fraction increases to 99.6% when only bright sources ( $K_S < 24$ ) are considered. We also extracted a  $K_S$  band detected catalog, and verified that all the objects detected in the

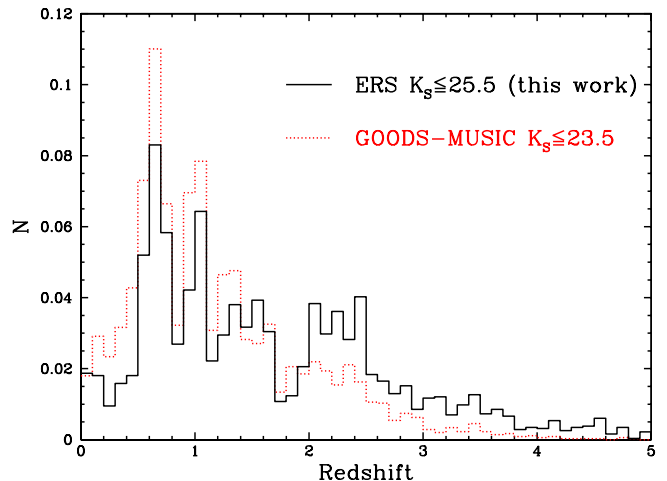


**Fig. 1.** Redshift distribution of the  $K_S \leq 25.5$  GOODS-ERS sample (black solid histogram) compared to the  $K_S \leq 23.5$  GOODS-MUSIC one adopted by Fontana et al. (2006) (red dotted histogram). Overdensities at  $z \simeq 0.7$ ,  $z \simeq 1$ ,  $z \simeq 1.6$  and  $z \simeq 2.2 - 2.3$  can be recognized in the distribution (see text for references).

$K_S$  band are also detected in the  $H$  one, which is not surprising given the extraordinary quality of the WFC3 data.

Based on these results we decided to restrict our analysis to the  $K_S \leq 25.5$  sample, albeit obtained from the  $H$ -selected one, for two reasons: firstly, this selection allows a better comparison with previous  $K$ -selected surveys; secondly, a  $K_S = 25.5$  threshold is more efficient in detecting low mass objects compared to a  $H = 26$  one. Adopting this cut, we extend by two magnitudes the previous work of Fontana et al. (2006), who studied the GSMF on the  $K_S < 23.5$  GOODS-MUSIC sample. The  $K_S \leq 25.5$  sample includes 3210 objects, 421 of which with spectroscopic redshifts.

We plot in Fig. 1 the redshift distribution of the GOODS-ERS sample used in this work compared to the GOODS-MUSIC one adopted by Fontana et al. (2006). Since the area covered by the ERS survey is relatively small, the sample is more sensitive to overdensities. The extended overdensities at  $z \simeq 0.7$  and  $z \simeq 1$  which cover in the entire GOODS-S field (Vanzella et al. 2005, Salimbeni et al. 2009a and references therein) are clearly recognizable. Unfortunately, the northern part of GOODS-S also includes a cluster at  $z \simeq 1.6$  (Castellano et al. 2007) and various groups at  $z \simeq 2.2 - 2.3$  (Salimbeni et al. 2009a; Yang et al. 2010; Magliocchetti et al. 2011), both affecting the overall redshift distribution.

Another difference with respect to Fontana et al. (2006) analysis is that the final sample used in this work includes Type 2 AGNs, since we show in Santini et al. (2011) that their stellar mass estimate is not significantly affected by the nuclear emission. The same is not true for Type 1 AGNs (Santini et al. 2011), so we removed spectroscopically identified Type 1 AGNs from the sample. Since their number is very low (only 4 sources identified in the entire sample), their removal does not affect the GSMF estimate. We also removed all identified Galactic stars. Finally, we applied a redshift selection in the range 0.6–4.5 and we end up with a sample of 2709 objects (of which 354 have spectroscopic redshifts).

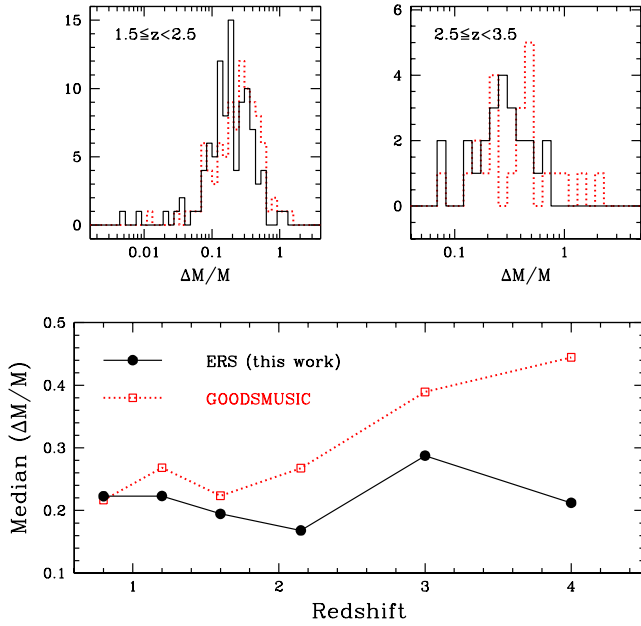


**Fig. 2.** *Upper* Distribution of the  $\Delta M/M$  ratio, where  $\Delta M$  is the average  $1\sigma$  error bar for each object, at  $z \sim 2$  (left) and  $z \sim 3$  (right). Black solid histograms refer to the GOODS-ERS sample, red dotted ones show GOODS-MUSIC data set. *Lower* Median  $\Delta M/M$  in each of the redshift bins used in this work as a function of the central redshift for GOODS-ERS (black solid circles/solid lines) and GOODS-MUSIC (red open boxes/dotted lines).

### 3. The stellar mass function

#### 3.1. Stellar masses

Stellar masses were estimated by fitting the 14 bands photometry (up to  $5.5 \mu\text{m}$  rest-frame) to the Bruzual & Charlot synthetic models, in both their 2003 (BC03 hereafter) and 2007 version (Bruzual 2007, CB07), through a  $\chi^2$  minimization. For consistency with our previous works and with most of the studies in the literature, we adopt the estimates derived with BC03 templates as the reference ones. In the fitting procedure, redshifts were fixed to the spectroscopic or photometric ones.  $1\sigma$  errors, due both to photometric uncertainties and to the photometric redshifts scatter, were computed by considering all the solutions within  $\chi^2_{\min} + 1$ . During the error computation, spectroscopic redshifts were fixed to their value while photometric ones were left free to vary around their best fit solution in order to account for their degeneracy.

We parametrized the star formation histories as exponentially declining laws with timescale  $\tau$ . We used a wide parameter space for metallicities, ages, extinctions,  $\tau$ , whose details can be found in Fontana et al. (2004), updated as in Santini et al. (2009). With respect to our previous works, we also excluded templates with super-solar metallicity at  $z \geq 1$ . Studies on the mass-metallicity relation (Maiolino et al. 2008) indeed demonstrated that galaxies at high redshift are typically characterized by sub-solar metallicities. We decided to adopt exponentially declining  $\tau$  models despite the fact that they likely are a poor and oversimplified description for the star formation history (e.g., Maraston et al. 2010). However, Lee et al. (2010) showed that the resulting stellar masses can still be considered robust due to

a combination of effects in the estimate of the galaxy star formation rates and ages. Moreover,  $\tau$ -models are widely used even in the most recent literature and allow a direct comparison with previous works.

We adopted a Salpeter IMF. We also computed the stellar masses by assuming a Chabrier IMF, and we checked that these are simply shifted by a factor  $-0.24$  dex, which is constant within 3% at the different redshifts. Moreover, we tested that the stellar mass functions obtained by adopting the two IMFs are consistent after applying the same shift, in agreement with what found by Salimbeni et al. (2009b).

The comparison with our previous GOODS-MUSIC sample allows us to test the effect of a deeper photometry on the accuracy of photometric redshifts and stellar masses. For this reason we compare photometric redshifts and stellar masses on the very same objects. The photometric redshifts of the present GOODS-ERS data are in very good agreement with the GOODS-MUSIC ones. Considering all objects in common between the two catalogs, the average scatter is  $<|z_{\text{ERS}} - z_{\text{GOODS-MUSIC}}|/(1 + z_{\text{ERS}})> = 0.07$ , with only 0.06% of severe (scatter  $> 0.5$ ) outliers. Stellar masses are also consistent with those derived from the GOODS-MUSIC catalog. When selecting galaxies for which the redshift estimate differs by 0.1 at most, the scatter  $(M_{\text{ERS}} - M_{\text{GOODS-MUSIC}})/M_{\text{ERS}}$  is on average equal to  $-0.03 \pm 0.40$ . The major improvement due to the higher quality photometry of WFC3 observations is the reduction of the uncertainties on the stellar masses. In Fig. 2 we compare the relative error on the stellar mass estimated using GOODS-ERS data set (black solid circles/solid lines) with that obtained from GOODS-MUSIC catalog (red open boxes/dotted lines). Again, we selected only galaxies common to both catalogs with consistent redshifts. In the upper panels we show the distribution of the  $\Delta M/M$  ratio, where  $\Delta M$  is the average  $1\sigma$  error bar for each object ( $\Delta M = (M_{\text{max}} - M_{\text{min}})/2$ ), in two redshift intervals centred at  $z = 2$  and  $z = 3$ ; in the lower panel we plotted, as a function of redshift, the median  $\Delta M/M$  in each of the redshift bins used in this work. Relative errors on the stellar mass for the GOODS-ERS sample are on average  $\sim 30\%$  lower than those computed on the same objects using the GOODS-MUSIC photometry, the difference increasing with redshift. It is clear that deep photometry in the near-IR regime is crucial to improve stellar mass estimates.

#### 3.2. The GSMF estimate

We estimated the stellar mass function by adopting both the non-parametric  $1/V_{\max}$  method (Schmidt 1968) and the STY (Sandage et al. 1979) maximum likelihood analysis assuming a Schechter parametric form. Like any other magnitude-limited sample, our sample does not have a defined limit in stellar mass. For this reason, at each stellar mass and at each redshift, we computed the fraction of objects lost because of the width of the  $M_*/L$  distribution by adopting the technique described in Fontana et al. (2004), after verifying that the simple parametrization used to describe the observed  $M_*/L$  distribution still holds for our sample.

We show the results of our analysis as black solid circles ( $1/V_{\max}$  method) and black solid lines (STY approach) in Fig. 3 (where the reference BC03 templates were used). The best fit Schechter parameters are reported in Tab. 1. Error bars on the  $1/V_{\max}$  points include Poissonian uncertainties as well as uncertainties on the stellar masses. The latter were estimated by means of a Monte Carlo simulation, where we randomly extracted the stellar masses according to their  $1\sigma$  uncertainties and

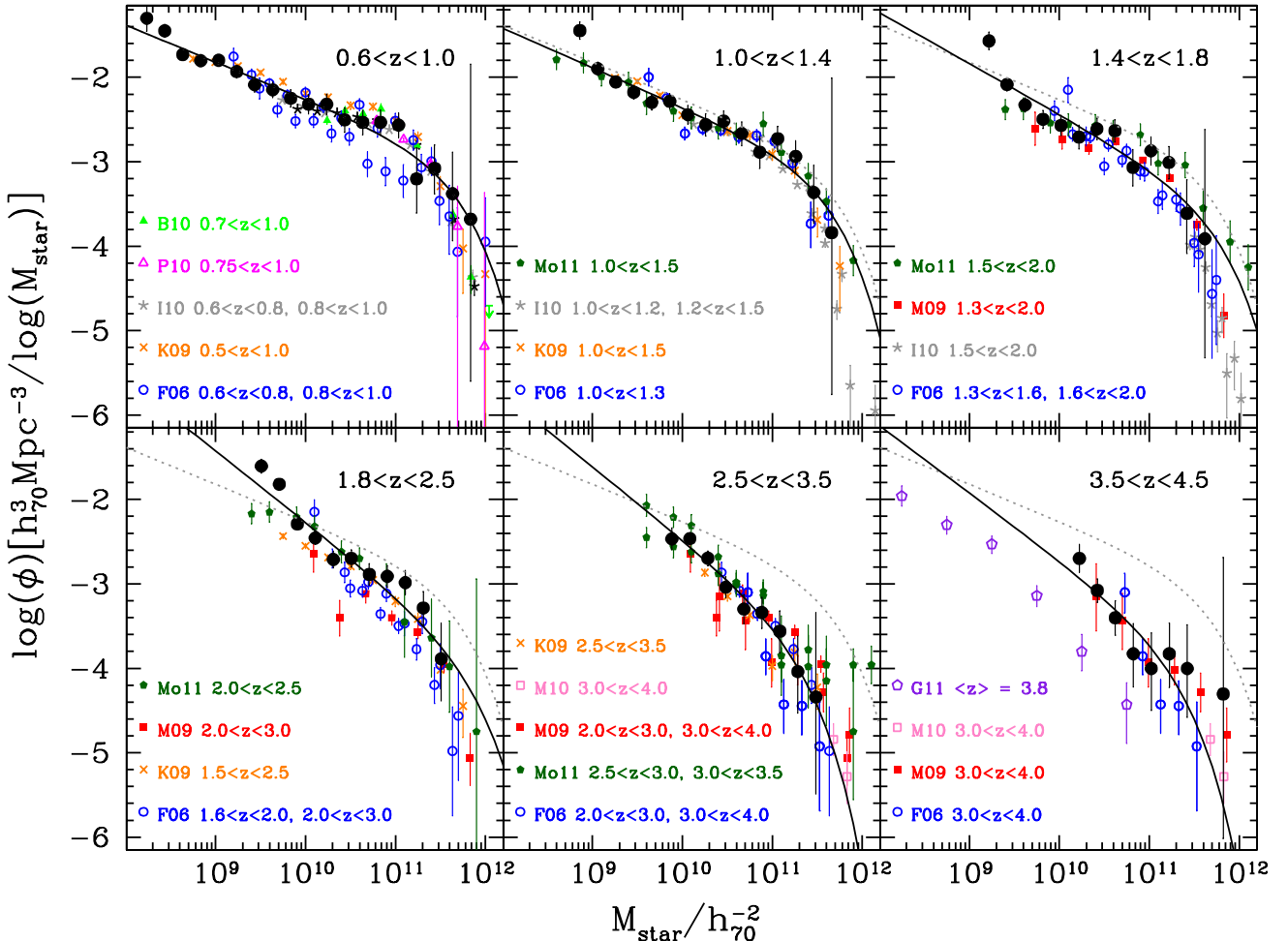


**Fig. 3.** Stellar mass functions obtained with BC03 stellar templates in different redshift ranges compared with previous works. Black solid circles represent our analysis with the  $1/V_{max}$  method, black solid lines show the best fit to a Schechter function according to the STY approach. The gray dotted line replicates the best fit Schechter function at  $z \sim 0.8$  in the higher redshift panels. Error bars include the uncertainties on the stellar masses as well as Poissonian errors. The highest mass points are often poorly determined, because of the large statistical error, resulting from our poor sampling of the massive side. Other symbols present  $1/V_{max}$  results of previous works, scaled to the same cosmology and converted to the same IMF: Fontana et al. (2006): open blue circles (F06); Bolzonella et al. (2010): solid green triangles (B10); Pozzetti et al. (2010): open purple triangles (P10); Ilbert et al. (2010): gray stars (I10); Kajisawa et al. (2009): orange crosses (K09); Marchesini et al. (2009): solid red boxes (M09); Marchesini et al. (2010): open pink boxes (M10); Mortlock et al. (2011): solid dark green pentagons (Mo11); González et al. (2011): open violet pentagons (G11). All the literature works considered for the comparison adopt the same stellar templates as this study. The legend shows the redshift intervals in which each set of points was computed.

re-computed the GSMF on 10000 mock catalogs using the same procedure described above.

Given the degeneracy between the faint-end slope  $\alpha$  and the characteristic mass  $M^*$  of the Schechter function, the STY approach suffers from the incomplete sampling of the high mass regime due to our small area, especially at high redshift. For this reason the highest mass  $1/V_{max}$  points are often poorly determined, because of the large statistical error. In the highest redshift bin, in order to constrain the fit, we fixed<sup>1</sup>  $M^*$  to the value obtained at  $z \sim 3$ . The fits found in this case are shown in Fig. 3 and the relevant Schechter parameters are given in Tab. 1. In this table we also provide (third column) the fraction

of objects where a secondary photometric redshift solution falls outside each redshift interval. This fraction is defined following the criterion discussed above and allowing a tolerance in photometric redshift of 0.2. We find an evolution in the number density, as given by the normalization parameter  $\phi^*$ , which decreases with increasing redshift from  $10^{-3.70^{+0.06}}_{-0.07}$  at  $z \sim 0.8$  to  $10^{-4.12^{+0.08}}_{-0.10}$  at  $z \sim 4$ . We remind that cosmic variance effects could cause oscillations in the normalization parameter, especially in the two bins which are most affected by the presence of overdensities, namely the 1.4 – 1.8 and 1.8 – 2.5 redshift intervals. However, a similar decreasing trend for the normalization was also observed by previous works (e.g. Fontana et al. 2006; Pérez-González et al. 2008; Kajisawa et al. 2009; Marchesini et al. 2009; Mortlock et al. 2011). Most interestingly, the low mass slope steepens significantly from  $z \sim 0.8$

<sup>1</sup> In Sect. 4 we study how the best fit parameter  $\alpha$  varies when choosing a different value for  $M^*$ .

to  $z \sim 3$ , with the Schechter parameter  $\alpha$  decreasing from  $-1.44 \pm 0.03$  to  $-1.86 \pm 0.16$ , and it flattens from  $z \sim 3$  to  $z \sim 4$ . As demonstrated in Sect. 4, this result keeps its validity despite the uncertainties deriving from the small area covered by our survey and the presence of known overdensities. Indeed, even the redshift ranges most contaminated show faint-end slopes in line with the results in the other redshift bins.

Up to  $z \sim 2.5$  the stellar mass function shows a dip at  $M_* \approx 10^{10} M_\odot$ , which seems to shift to higher stellar masses as redshift increases, making a single Schechter a poor parametrization. Such a dip was identified in previous wide field surveys and it was interpreted as due to the differential evolution of the red and the blue populations (Ilbert et al. 2010; Pozzetti et al. 2010; Bolzonella et al. 2010; Mortlock et al. 2011). The effect is larger in the redshift intervals  $1.4 < z < 1.8$  and  $1.8 < z < 2.5$ , which are highly affected by the presence of a well-known cluster at  $z \sim 1.6$  (e.g. Castellano et al. 2007) and of a number of localized overdensities at  $z \approx 2.2 - 2.3$  (Salimbeni et al. 2009a; Yang et al. 2010), respectively: they are indeed populated by a higher fraction of old red galaxies, which enhances this dip. A different explanation for the dip around  $\sim 10^{10} M_\odot$  was suggested by Drory et al. (2009), who measured a bimodal shape also in the GSMF of the blue and red populations separately. This dichotomy in galaxy formation which pre-dates the red sequence appearance was ascribed to a change with stellar mass either in star formation efficiency or galaxy assembly rate. The studies cited above show that a double Schechter is a better description of the shape of the total GSMF. However, given the small size of our sample, the inclusion of two more free parameters (Bolzonella et al. 2010) makes the fit degenerate and was not applied here.

### 3.3. Comparison with previous results

We show in Fig. 3 a compilation of  $1/V_{max}$  points collected from the literature, as listed in the legend, scaled to the same cosmology and IMF. Unfortunately, it is not possible to correct for the effect of different stellar libraries, since, as we show in the next section, they do not determine a systematic shift which can be applied on the GSMF. Therefore, we decided to show only those studies which adopt the same stellar library as this work. Overall, our results are in good agreement with most of the other surveys, especially up to  $z \sim 3$ . In the two redshift intervals affected by the overdensities ( $z \sim 1.6$  and  $z \sim 2.2$ ), our GSMF are on average higher than the other surveys, but still consistent with most of them within the errors. In general, we report a larger number of galaxies at the bright tail with respect to Fontana et al. (2006): this is due to the fact that the present study includes AGNs (except the few identified Type 1), which preferentially live in high mass galaxies (Bundy et al. 2008; Alonso-Herrero et al. 2008; Brusa et al. 2009; Silverman et al. 2009; Xue et al. 2010). Given the very deep near-IR observations used in this work, the sampling of the low-mass-end of the GSMF is considerably improved with respect to most previous surveys, on average by 0.5 dex up to  $z \sim 1.8$  and by 0.1 dex at  $z \sim 4$ , and at the same time the conservative photometric cut ( $K_S < 25.5$ ) ensures reliable results even at the lowest masses.

The only comparable study sampling similar or slightly lower stellar masses is the one by Mortlock et al. (2011). This work is somewhat peculiar, being obtained from a set of biased pointings specifically designed to contain as many massive galaxies as possible, and a posteriori corrected to account for this bias. They push the detection to  $H = 26.8$  at a  $5\sigma$  level, while our sample, although extracted from images of similar depth,

is cut at a brighter limit in order to ensure good photometric quality. Also, they do not include a  $K$  band, which is important to estimate reliable stellar masses. Finally, being based on a 14 bands photometry (instead of 6 bands as Mortlock et al. 2011), our work also relies on good quality photometric redshifts.

Despite the limited sky area, the bright-end tail is overall comparable within the uncertainties with that inferred by large surveys over the whole redshift range (with the exception of the  $1.4 - 2.5$  redshift interval, which, as discussed above, is affected by the presence of overdensities). The only severe disagreement is found when comparing our results in the highest redshift interval to González et al. (2011), who, as already pointed out in the introduction, derived the GSMF by using a different procedure, i.e. by combining the UV luminosity function with an average  $M_*/L$  ratio.

### 3.4. The effect of different stellar templates

Systematic uncertainties due to the various assumptions involved in spectral energy distribution modelling were demonstrated to dominate the overall error budget affecting the GSMF (see Marchesini et al. 2009, for a detailed analysis). In this regard, a significant role is played by the choice of the stellar templates used to estimate the stellar mass.

Stellar masses obtained through the CB07 stellar library, which include an improved TP-AGB stars treatment, are on average 0.12 dex smaller than those inferred through the BC03 templates, with a scatter as large as 0.17 dex. We plot in Fig. 4 their ratio as a function of the stellar mass adopted as reference in this work ( $M_{BC03}$ ) in different redshift bins. The lack of a clear trend of  $M_{BC03}/M_{CB07}$  with stellar mass or redshift translates into a lack of rigid offset between the GSMF computed with the two libraries, although the CB07 points are on average at lower stellar masses than BC03.

We present in Fig. 5 the comparison between GSMF obtained with the BC03 templates (black solid curves/solid circles) and the CB07 ones (red dotted curves/open boxes). For the sake of simplicity, we decided to report the four most representative bins. The  $1.0 - 1.4$  and  $1.4 - 1.8$  redshift bins are very similar to the  $0.6 - 1.0$  and  $1.8 - 2.5$  ones, respectively. We also show the  $1/V_{max}$  points from Marchesini et al. (2009) (their Set 8) and Caputi et al. (2011), both obtained by adopting the CB07 templates. The results of Marchesini et al. (2009) agree with our CB07-based GSMF in all except in the  $1.8 - 2.5$  redshift interval, likely because of non perfect redshift overlap between the two analysis. The points from Caputi et al. (2011) are in broad agreement with ours at the bright end, while incompleteness that the authors claim below  $M_* \sim 10^{11} M_\odot$  is likely responsible for the disagreement at low stellar masses.

The best fit Schechter parameters of the CB07-based GSMF are reported in Tab. 2. At  $z > 2.5$  we were forced to fix<sup>2</sup> the  $M^*$  parameter to its best fit value at  $z \sim 2.15$ . If it is instead set free, the fit is unconstrained or the maximum likelihood analysis does not converge. The CB07- and BC03-based GSMF differ between each other. However, we do not measure a similar systematic behaviour at all redshifts. The fact that the high-mass end of the CB07-based GSMF is unconstrained at  $z > 2.5$ , while the BC03-based one suffers from poor statistical sampling only in the highest redshift bin ( $z > 3.5$ ), is a further confirmation that the two GSMF are not the result of a simple shift in the stellar mass.

<sup>2</sup> See Sect. 4 for an analysis of how the best fit parameter  $\alpha$  varies when choosing a different value for  $M^*$ .

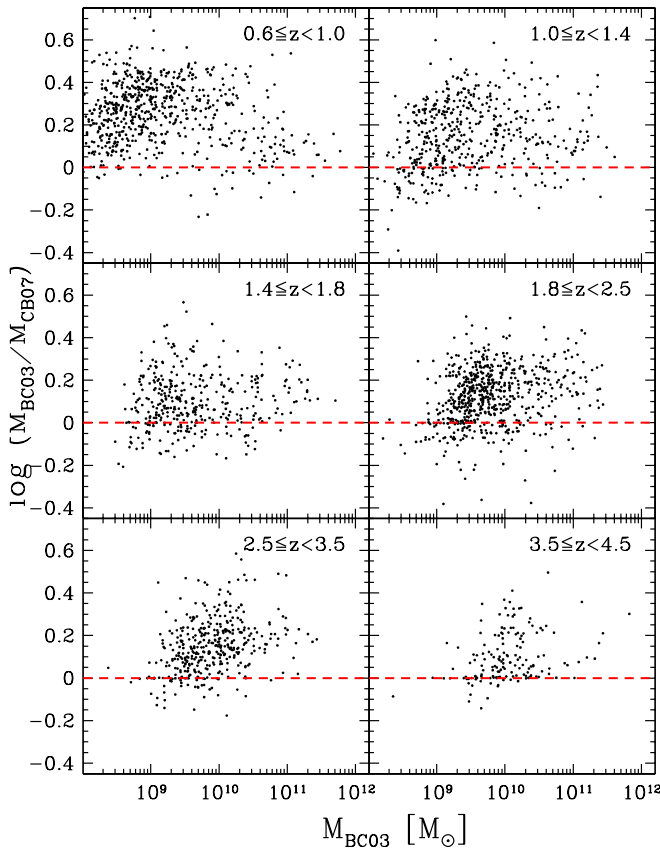


**Fig. 4.** Ratio between stellar masses computed with BC03 ( $M_{BC03}$ ) and CB07 ( $M_{CB07}$ ) templates versus  $M_{BC03}$  in different redshift bins.

At the lowest and the highest redshifts we find the better agreement, the normalization of the best fit Schechter function being only slightly lower when CB07 templates are used. At intermediate redshifts we observe a more serious disagreement, resulting in different faint-end slopes and characteristic masses. This is not surprising, since the effect of the inclusion of the TP-AGB phase is expected to be important at intermediate ages (0.2 – 2 Gyr), which predominate the  $2 \leq z \leq 3$  redshift range (Maraston 2005; Henriques et al. 2011). Although the difference between the CB07- and the BC03-based GSMF do not show a systematic trend at all redshifts, the characteristic masses seem to be on average smaller when CB07 templates are used (see Fig. 6 discussed in the next section), as expected, despite the large uncertainties, in agreement with the results of Marchesini et al. (2009). This trend is clear at  $1.4 < z < 2.5$ , where our redshift bins overlap with those of Marchesini et al. (2009), while the lack of statistics at higher redshifts prevents us to draw any firm conclusion about the effect of changing the stellar templates. For what concerns the variation in  $\alpha$  when changing the template library, we find similar slopes from  $z \sim 0.8$  to  $z \sim 1.2$ , while in the redshift interval  $1.4 - 2.5$  the BC03-based GSMF are steeper than the CB07-based ones by 0.2 – 0.3. Marchesini et al. (2009) reports similar slopes when using BC03 and CB07 stellar templates in the redshift interval  $1.3 - 3.0$ , while their BC03-based GSMF is steeper than the CB07-based one at  $3.0 < z < 4.0$ . The intrinsic difference between the two surveys does not allow to investigate the origin of this mismatch.

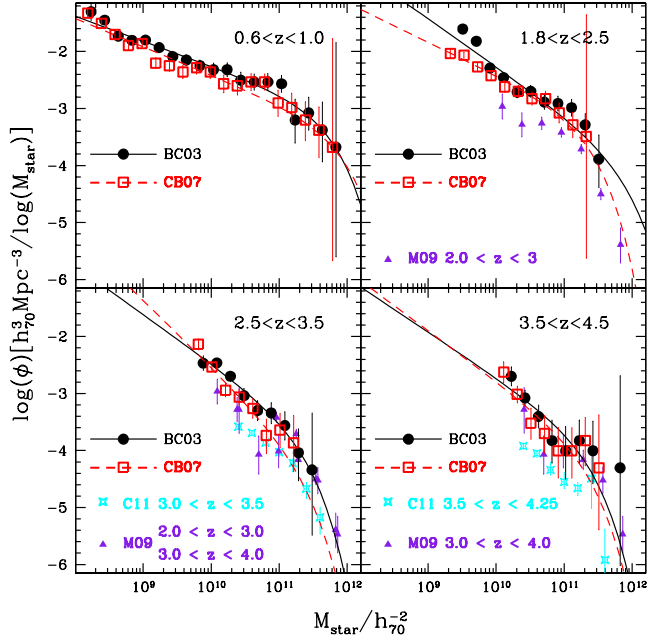


**Fig. 5.** Comparison between the stellar mass functions obtained with Bruzual & Charlot (2003) template library (black solid circles and solid curves) and with the Bruzual (2007) one (red open boxes and dashed curves). Symbols are the results of the  $1/V_{max}$  analysis and curves represent the STY Schechter fits. Error bars include the uncertainties on the stellar masses as well as Poissonian errors. Other symbols present  $1/V_{max}$  results of previous works based on CB07 templates, scaled to the same cosmology and converted to the same IMF: Marchesini et al. (2009): solid purple triangles (M09); Caputi et al. (2011): cyan stars.

#### 4. The faint-end slope

The main goal of this study is to investigate the faint-end slope of the GSMF, especially at the highest redshifts ( $z > 2$ ). Both from Fig. 3 and from Tabs. 1 and 2 it is evident that the low mass tail steepens with redshift. Results from the STY approach on our BC03-based data indicate that the faint-end slope steepens significantly from  $z \sim 0.8$ , where we fitted  $\alpha = -1.44 \pm 0.03$ , to  $z \sim 3$ , where the best fit  $\alpha$  is equal to  $-1.86 \pm 0.16$ , and it flattens up to  $z \sim 4$ .

First of all, we perform a simple sanity check to verify that the abundance of low mass objects at  $z > 1.8$  is reliable by plotting all objects with  $M_* < 10^{10} M_\odot$  and  $1.8 < z < 2.5$  on a  $BzK$  diagram. For galaxies at  $z > 2.5$  we adopted the analogous  $RJL$  diagram (using IRAC  $3.6 \mu\text{m}$  as  $L$  band), which extends the former to the  $2.5 < z < 4$  redshift regime (Daddi et al. 2004), and checked stellar masses below  $2 \cdot 10^{10} M_\odot$ . Approximately 91% of the sources indeed lie in the high redshift regions of these diagrams, making us confident of their photometric redshift estimate. As a further check, we carefully inspected the individual photometric redshift probability distribution curves for each source with  $z > 1.8$  and  $M_* < 2 \cdot 10^{10} M_\odot$ . Following the criterion described in Sect. 2, we find that 96.5% of these sources have a 90% probability of lying at  $z > 1.5$ .

As already pointed out in Sect. 3.2, the small sky area sampled by our data may be responsible for degeneracies between the faint-end slope  $\alpha$  and the characteristic mass  $M^*$  when fitting a Schechter function. We therefore study in detail the degenera-

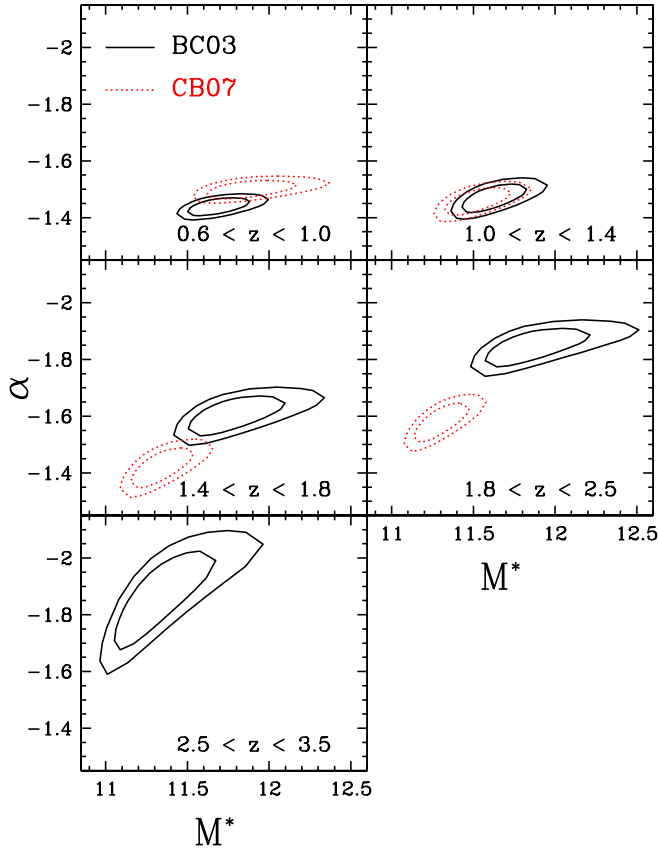


**Fig. 6.**  $\alpha$  and  $M^*$  space ( $1\sigma$  and  $2\sigma$  contours) resulting from the maximum likelihood analysis. Black solid curves refer to BC03-based GSMF, red dotted curves refer to CB07-based ones.

cies in the  $\alpha - M^*$  plane. The results are shown in Figs. 6 and 7. In the first figure we analyse the redshift intervals where both parameters are set free, while in the second one we study the dependence of the best fit  $\alpha$  on the chosen  $M^*$  in those redshift bins where we were forced to fix the characteristic mass in order to constrain the maximum likelihood analysis.

In Fig. 6 we show the  $1\sigma$  and  $2\sigma$  contours for  $\alpha$  and  $M^*$  Schechter parameters, for both BC03-based GSMF (black solid curves) and CB07-based ones (red dotted curves). While the parameter  $\alpha$  is well constrained at all redshift (although with uncertainties increasing with  $z$ ), our data prevent us to properly infer the value of the characteristic mass. Nonetheless, as we show below, the result on  $\alpha$  is robust against the degeneracy of  $M^*$ .

The steepening of  $\alpha$  from  $z \sim 0.8$  to  $z \sim 3$  is clear from Fig. 6 when the BC03 stellar library is used. If instead adopting CB07 templates, the faint-end slope does not change much from  $z \sim 0.8$  to  $z \sim 2.2$ , while at higher redshifts ( $2.5 < z < 3.5$ ) we were forced to fix the value of  $M^*$  to constrain the fit (see Sect. 3.4), making the best fit  $\alpha$  parameter dependent on the choice of the characteristic mass.

In order to study how the best fit value of  $\alpha$  changes when varying the  $M^*$  value, we built a grid of  $\log(M^*[M_\odot])$  ranging from 10.5 to 11.6 (these limits are justified by previous works) with step of 0.1 and we fit a Schechter function to the data for each element of the grid. We adopted this procedure in all the redshifts bins where the fit is unconstrained. We show in Fig. 7 the  $\alpha - M^*$  plane, where the shaded areas show the values of the

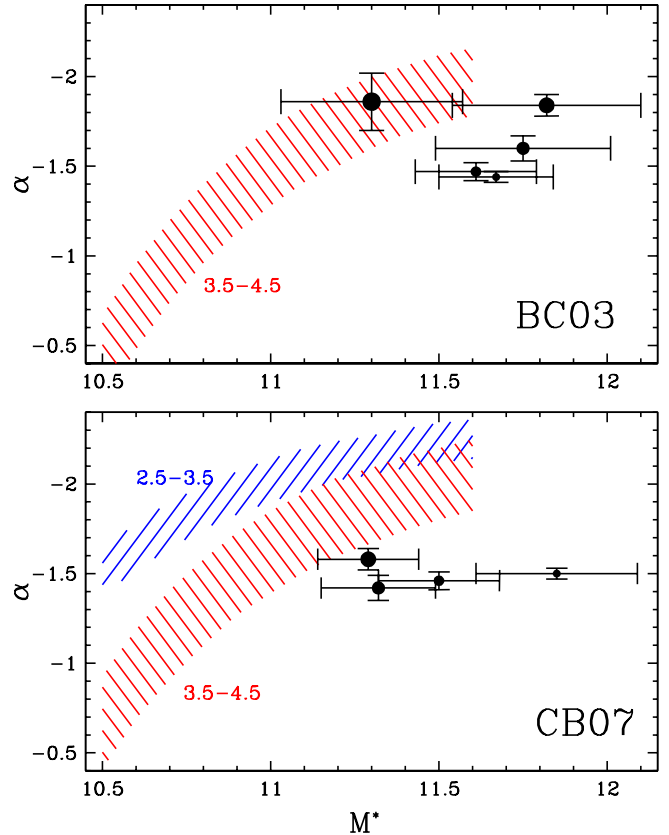


**Fig. 7.** Best fit  $M^*$  and  $\alpha$  parameters obtained by adopting BC03 (upper panel) and CB07 (lower panel) templates at different redshifts. The symbol size increases with redshift. The shaded areas show the values of the faint-end slope at different fixed  $M^*$  in the redshift bins indicated by the labels.

faint-end slope at different fixed  $M^*$  in the redshift bins indicated by the labels. The symbols show the best fit values (and their uncertainties) for  $\alpha$  and  $M^*$  at  $z < 3.5$  ( $z < 2.5$  when using CB07 templates), where our results are not significantly affected by the lack of statistics and we could set both parameters free. The upper panel refers to the BC03-based GSMF while the lower one is obtained by adopting CB07 stellar templates.

From Fig. 7 (lower panel, blue shaded region) it appears that, whatever reasonable value for  $M^*$  is chosen at  $2.5 < z < 3.5$ , the best fit  $\alpha$  clearly steepens compared to its best fit values at lower redshifts, confirming what found with BC03 templates and supporting that the major result of this paper is not affected by the poor sampling of the high mass regime. However, as shown by the red shaded regions in Fig. 7, present data prevent us to draw any firm conclusion about the trend of  $\alpha$  between  $z \sim 3$  and  $z \sim 4$ .

To further corroborate the result on the slope of the low-mass-end, and definitely make sure that is not affected by the lack of statistics at the massive end, we took advantage from the outcomes of large surveys and followed different approaches. We fitted the  $1/V_{max}$  points from this study together with those collected from the literature in comparable redshift intervals. We note that in principle, contrary to the STY approach, fitting  $1/V_{max}$  points involves data binning, and thus may in general produce a different fit. We included only those surveys whose

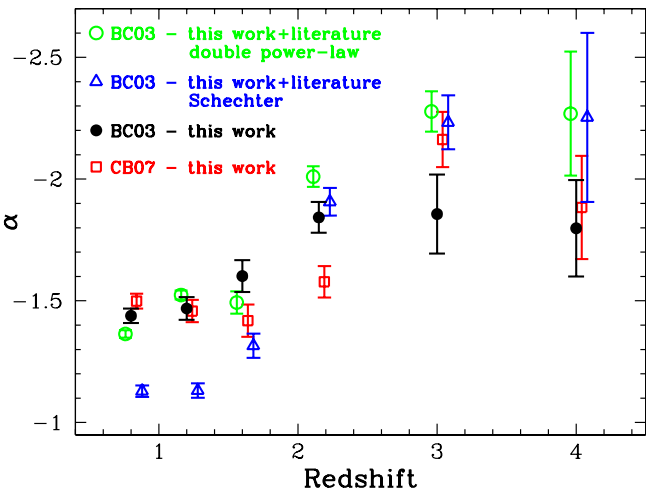


**Fig. 8.** Faint-end slope as a function of redshift. The parameter  $\alpha$  was computed through a maximum likelihood analysis with a Schechter form (black solid circles refer to the BC03 library, red open boxes refer to the CB07 one) and by fitting the ensemble (this study + previous surveys) of  $1/V_{max}$  points with a Schechter parametric form (blue open triangles) and a double power-law shape (see text, green open circles). The different sets are shifted in redshift with respect of the central values in each interval (shown by the solid black circles).

results are obtained using a method similar to our own and which sample the high mass tail of the distribution, typically above  $M_* \simeq 3 \times 10^{10} M_\odot$ . However, we obtained very similar results when including also the points from the literature at lower masses. We found that a single Schechter function does not seem to reproduce the faint- and the bright-end at the same time in a satisfactory way. This is not surprising since the Schechter function is itself a poor description of the shape of the GMSF when samples with high statistics are used (see discussion in the introduction and in Sect. 3.2). However, the non homogeneity of the data set can also play a role: we collected  $1/V_{max}$  points from different surveys, observing different sky areas, and computed with slightly different methods. We then fitted the ensemble of the  $1/V_{max}$  points from this work plus those collected from the literature with a double power-law<sup>3</sup>. The best fit parameters are shown in Tab. 3. This analytic shape, having one more degree of freedom, produces a better fit to the data at all redshifts.

We report the different values of the faint-end slope as a function of redshift in Fig. 8. It is shown that, whatever stellar templates and method are adopted and whatever functional shape is fitted to the data, all the results indicate a steepening of the faint-end of the GMSF with redshift up to  $z \sim 3$ . The trend is robust despite the relatively large error bars, especially at high redshift, and the presence of known overdensities at  $z \sim 1.6$  and  $z \sim 2.2 - 2.3$ , and it is not affected by the lack of statistics at the high-mass-end which characterizes small sky areas. The steepening of the faint-end slope seems to halt at  $z > 3$  and the value of  $\alpha$  seems to remain constant up to  $z \sim 4$ . However, although this is confirmed by the use of the outcome of previous large surveys, the results based on our data alone are largely dependent on the choice of the fixed  $M^*$  parameter.

The tendency for the low-mass-end of the GMSF to steepen with redshift was already found by previous authors. According

to the evolutionary STY fit of Fontana et al. (2006),  $\alpha$  ranges from  $-1.25 \pm 0.03$  at  $z \sim 0.8$  to  $-1.51 \pm 0.13$  at  $z \sim 4$ . Increasing but flatter values for the faint-end slope were obtained by Marchesini et al. (2009), who reported  $\alpha = -0.99$  at  $z \sim 1.6$  and  $\alpha = -1.39$  at  $z \sim 3.5$ . Kajisawa et al. (2009) found  $\alpha = -1.26^{+0.03}_{-0.03}$  at  $z \sim 0.75$  and  $\alpha = -1.75^{+0.15}_{-0.13}$  at  $z \sim 3$ . Very steep GMSF, in agreement with those inferred with our data, were fitted by Caputi et al. (2011), who measured  $\alpha = -2.07^{+0.08}_{-0.07}$  at  $z \sim 3.9$ . Finally, Mortlock et al. (2011) reported  $\alpha = -1.36 \pm 0.05$  at  $z \sim 1.25$  and  $\alpha = -1.89 \pm 0.11$  at  $z \sim 2.75$ . Both Mortlock et al. (2011) and Caputi et al. (2011) found a flattening at higher redshift similar to the one that we measure at  $z \sim 4$ , i.e. they fitted  $\alpha = -1.73 \pm 0.09$  at  $z \sim 3.25$  and  $\alpha = -1.85^{+0.27}_{-0.32}$  at  $z \sim 4.6$ , respectively.

We note that the equally robust results can not be inferred for the evolution of the characteristic mass  $M^*$ , whose best fit values are highly sensitive to the stellar templates and to the functional shape fitted to the data (see Tabs. 1, 2 and 3), as well as to the size of the sample.

## 5. The stellar mass density

We computed the total stellar mass density by integrating the analytical fitting functions in each redshift bin from  $10^8$  to  $10^{13} M_\odot$ . We show in Fig. 9 the SMD derived from the STY analysis using BC03 and CB07 templates as solid black and red curves respectively. We also show a compilation of results from the literature, reported to the same cosmology and IMF, as listed in the legend. The same integration limits as in this study were used in most of the works considered. The only exceptions are the Mortlock et al. (2011) points ( $M_* > 10^7 M_\odot$ ), the Ilbert et al. (2010) ones ( $M_* > 10^5 M_\odot$ ), and those from Dickinson et al. (2003) and Pérez-González et al. (2008), who adopted redshift-dependent mass limits (we refer to these works for more details). Our results show good agreement with those computed by previous authors at  $0.6 \leq z \leq 2$ , although we remind once again that our redshift intervals around  $z \sim 1.6$  and  $z \sim 2.2 - 2.3$  could be biased high by a few known overdensities. The steepness of the faint-end of the GMSF computed by this work is responsible for the large values of the SMD inferred at  $z > 2$ . Our estimates are higher than those reported by previous authors, with the exception of the Mortlock et al. (2011) results. However, the latter originate from a different feature in the GMSF: Mortlock et al. (2011) indeed found flatter faint-end slopes than we do, and the large SMD is a consequence of a larger density of high mass galaxies (see Fig. 3).

It is also important to remark that the SMD still suffers from uncertainties due to systematic effects. In Fig. 9 the gray shaded region shows the dispersion of the SMD when including the outputs obtained from the integration of the fit of our  $1/V_{max}$  points + those collected from the literature with both a Schechter function and a double power law shape (see Sect. 4). This region represents the systematic errors deriving from the choice of the stellar library and of the functional shape for the GMSF, as well as from the simultaneous use of the ERS observations as a probe of the low mass end of the GMSF together with the results of large surveys to constrain the bright-end. The dispersion increases significantly at  $z \gtrsim 3$ , reflecting the large scatter among existing surveys. Moreover, the lack of overlapping with most previous results at these redshifts is a sign of the impossibility to assemble a single, self-consistent GMSF from the highest to the lowest masses. This is due to inhomogeneity of the samples, to the variance between different fields and also to the intrinsic uncertainties at high redshift on both stellar masses and GMSF.

<sup>3</sup> The assumed functional shape is  $\phi_* / [(M/M^*)^{-(1+\alpha)} + (M/M^*)^{-(1+\beta)}]$

Schechter parameters (STY method) – BC03 templates						
Redshift bin	N	% <sub>not secure</sub>	$\alpha$	$\log_{10}M^*(M_\odot)$	$\log_{10}\phi_*(\text{Mpc}^{-3})$	$\log \rho(M_\odot \text{Mpc}^{-3})$
0.6 - 1.0	584	8.5%	-1.44 $\pm$ 0.03	11.67 $\pm$ 0.17	-3.70 $^{+0.06}_{-0.07}$	8.51
1.0 - 1.4	375	6.2%	-1.47 $\pm$ 0.05	11.61 $\pm$ 0.18	-3.47 $^{+0.07}_{-0.08}$	8.35
1.4 - 1.8	259	9.7%	-1.60 $\pm$ 0.07	11.75 $\pm$ 0.26	-3.85 $^{+0.11}_{-0.14}$	8.23
1.8 - 2.5	425	7.4%	-1.84 $\pm$ 0.06	11.82 $\pm$ 0.28	-4.17 $^{+0.14}_{-0.20}$	8.29
2.5 - 3.5	182	11.8%	-1.86 $\pm$ 0.16	11.30 $\pm$ 0.27	-3.94 $^{+0.16}_{-0.16}$	7.97
3.5 - 4.5	51	8.4%	-1.80 $\pm$ 0.20	11.30 (fixed)	-4.12 $^{+0.08}_{-0.10}$	7.72

**Table 1.** Best fit Schechter parameters in the different redshift intervals as a result of the STY approach using Bruzual & Charlot (2003) templates. Parameters with no error bars have been fixed to the value in the lower redshift bin. The second column indicates the numbers of galaxies in each redshift bin based on which the GSMF is actually computed. The third column shows the fraction of galaxies where a secondary redshift solution outside the redshift bin can not be discarded with a 90% probability (see Sect. 3.2 for details). The last column reports the corresponding mass density  $\rho$  obtained by integrating the GSMF between  $10^8$  and  $10^{13} M_\odot$ .

Schechter parameters (STY method) – CB07 templates						
Redshift bin	N	% <sub>not secure</sub>	$\alpha$	$\log_{10}M^*(M_\odot)$	$\log_{10}\phi_*(\text{Mpc}^{-3})$	$\log \rho(M_\odot \text{Mpc}^{-3})$
0.6 - 1.0	509	8.5%	-1.50 $\pm$ 0.03	11.85 $\pm$ 0.24	-3.70 $^{+0.10}_{-0.13}$	8.39
1.0 - 1.4	372	6.2%	-1.46 $\pm$ 0.05	11.50 $\pm$ 0.18	-3.49 $^{+0.08}_{-0.09}$	8.22
1.4 - 1.8	264	9.7%	-1.42 $\pm$ 0.07	11.32 $\pm$ 0.17	-3.41 $^{+0.09}_{-0.12}$	8.09
1.8 - 2.5	437	7.4%	-1.58 $\pm$ 0.06	11.29 $\pm$ 0.15	-3.52 $^{+0.10}_{-0.12}$	8.07
2.5 - 3.5	153	11.8%	-2.16 $\pm$ 0.11	11.29 (fixed)	-4.39 $^{+0.28}_{-0.42}$	8.05
3.5 - 4.5	45	8.4%	-1.88 $\pm$ 0.21	11.29 (fixed)	-4.28 $^{+0.11}_{-0.15}$	7.67

**Table 2.** Same as Tab. 1 using Bruzual (2007) templates.

Double power-law parameters (fit to $1/V_{max}$ points) – BC03 templates					
Redshift bin	$\alpha$	$\beta$	$\log_{10}M^*(M_\odot)$	$\log_{10}\phi_*(\text{Mpc}^{-3})$	$\log \rho(M_\odot \text{Mpc}^{-3})$
0.6 - 1.0	-1.36 $\pm$ 0.02	-4.47 $\pm$ 0.12	11.39 $\pm$ 0.01	-2.75 $^{+0.02}_{-0.02}$	8.50
1.0 - 1.4	-1.52 $\pm$ 0.02	-5.24 $\pm$ 0.16	11.38 $\pm$ 0.01	-3.10 $^{+0.02}_{-0.02}$	8.24
1.4 - 1.8	-1.49 $\pm$ 0.05	-4.70 $\pm$ 0.23	11.30 $\pm$ 0.03	-3.12 $^{+0.05}_{-0.06}$	8.12
1.8 - 2.5	-2.01 $\pm$ 0.04	-6.25 $\pm$ 1.57	11.64 $\pm$ 0.06	-3.94 $^{+0.09}_{-0.12}$	8.28
2.5 - 3.5	-2.28 $\pm$ 0.08	-6.70 $\pm$ 4.84	11.77 $\pm$ 0.10	-4.73 $^{+0.17}_{-0.28}$	8.24
3.5 - 4.5	-2.27 $\pm$ 0.25	-6.38 $\pm$ 7.48	11.81 $\pm$ 0.19	-4.84 $^{+0.34}_{-4.84}$	8.15

**Table 3.** Best fit parameters of the double power-law shape fit to  $1/V_{max}$  points from this work (using BC03 templates) + a collection from the literature at  $M_* \gtrsim 3 \times 10^{10} M_\odot$  (see text). The last column reports the corresponding mass density  $\rho$  obtained by integrating the GSMF between  $10^8$  and  $10^{13} M_\odot$ .

We compared the stellar mass density with the integrated star formation rate density. For this purpose, we first considered the best fit to the compilation of SFRD measurements made by Hopkins & Beacom (2006). Following Wilkins et al. (2008), we rescaled it to a Salpeter IMF and integrated it as a function of time, after accounting for the gas recycle fraction. The latter is the fraction of stellar mass which is returned to the interstellar medium as a function of time, and was computed using Bruzual & Charlot (2003) model. The result of this calculation is shown in Fig. 9 by the blue dashed line. We then made the same calculation by using the best fit parametric shape for the star formation history inferred by Reddy & Steidel (2009), which includes also more recent high redshift points as well as a luminosity-dependent dust correction to the  $z > 2$  data. We obtained the green long dashed line shown in Fig. 9.

Our results solve the discrepancy between the SMD and the integrated SFRD at  $z > 2$  (modulo the uncertainties affecting the  $z \sim 2.1$  redshift interval), especially when considering the dispersion given by the inclusion of high mass  $1/V_{max}$  points from the other surveys. Consistency at high redshift was already

suggested by Mortlock et al. (2011) and by the recent work of Papovich et al. (2011), the latter based on a different analysis. Overall, our results support the notion that the SMD can be reasonably close to the integrated SFRD at  $z > 2$ , mostly due to a steepening of the GSMF, although our results can be biased high because of the known overdensities in the small ERS field. As mentioned, the higher values that we obtained with respect to most previous studies is essentially due to the efficiency of WFC3 deep near-IR data to accurately recover the faint-end of the stellar mass function, especially at high redshift, which contributes significantly to the total stellar mass density. However, the significant steepening in the faint-end slope presented in this work is not sufficient to solve the disagreement at  $z < 2$ , where the integrated SFRD exceeds the observed SMD by a factor of  $\sim 2 - 3$ , even when both of them are integrated down to low values of stellar mass / luminosity and adopting the SFRD computed by Reddy & Steidel (2009). The latter, although it makes the integrated SFRD lower than that resulting from the best fit of Hopkins & Beacom (2006) at  $z < 2.5$ , is still not able to reconcile the two observables. The discrepancy is not solved also

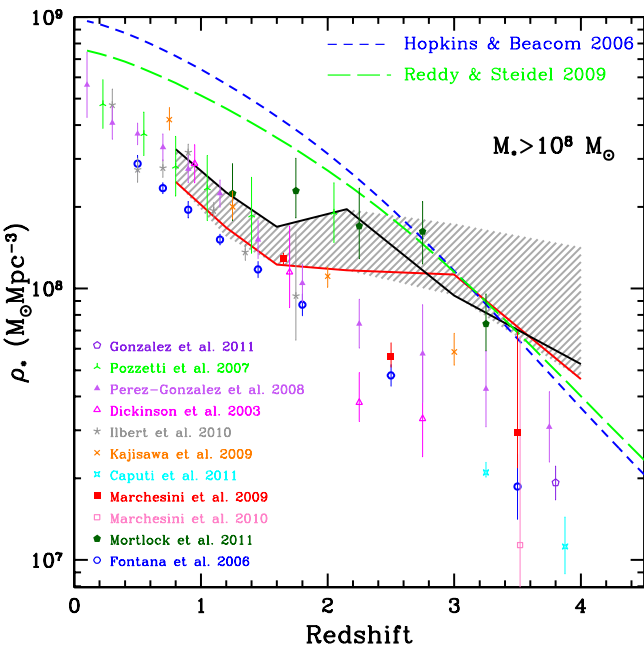


**Fig. 9.** Stellar mass density between  $10^8$  and  $10^{13} M_\odot$  versus redshift. The solid black and red curves are the integral of the STY Schechter fits using BC03 and CB07 templates, respectively. The gray shaded area shows the dispersion obtained when integrating the fit, with both a Schechter and a double power law functional shape, of our  $1/V_{max}$  points together with those from the literature (see text and Fig. 8). Coloured symbols represent a compilation of results from the literature as listed in the legend (see text for their integration limits). All the points are scaled to the same cosmology and IMF. All the results are based on BC03 stellar templates, except the Caputi et al. (2011) work, which adopts the CB07 library. As far as Marchesini et al. (2010) results are concerned, the central redshift was shifted by 0.02 for visualization purposes; given their Tab. 6, the central values is reported and the error bar indicates the total scatter of their estimates. The blue dashed and green long-dashed lines show the integrated star formation history according to the best fit from Hopkins & Beacom (2006) and Reddy & Steidel (2009), respectively.

when our deep data, which allow a good control of the faint-end slope, are matched to the large surveys results to constrain the bright tail of the GSMF, and it gets even worse if one assumes that our results are biased high given the features of the ERS field.

## 6. Comparison with theoretical models

We present in Fig. 10 the comparison of our results with the predictions of semi-analytical models of galaxy formation and evolution, which follow the evolution of the baryonic component by means of an approximate description of the relevant physical processes (i.e. gas cooling, star formation, stellar feedback, Black Hole growth and AGN feedback) and of their interplay with gravitational processes, linked to the assembly of the large-scale structure of the Universe. These “recipes” include a number of parameters which are usually fixed by comparing model predictions with a set of low-redshift observations. Despite their simplified approach, semi-analytical have turned

into a flexible and widely used tool to explore a broad range of specific physical assumptions, as well as the interplay between different physical processes. We considered different, independently developed semi-analytical models: Menci et al. (2006) (red dotted curves) updated to include the Reed et al. (2007) halo mass function, MORGANA (Monaco et al. 2007, as updated in Lo Faro et al. 2009, blue long-dashed curves), Wang et al. (2008) (green dashed curves) and Somerville et al. (2011) (orange dot-dashed curves). We refer to the original papers for a detailed description of the recipes adopted in the galaxy formation and evolution modelling. MORGANA, the Wang et al. (2008) and the Somerville et al. (2011) models resolve galaxies with  $M_* > 10^9 M_\odot$ , while the Menci et al. (2006) one has a lower mass limit of  $10^8 M_\odot$ . The predicted stellar masses were convolved with a Gaussian error distribution on  $\log M_*$  (see Fig. 2) in order to reproduce the observational uncertainties. We refer the reader to Fontanot et al. (2009) and Marchesini et al. (2009) for a detailed analysis on the effects of convolving the model predictions with observational errors. All stellar masses were converted to a Salpeter IMF.

We first compare the GSMF (upper panel of Fig. 10; we only plotted four redshift bins, the other two showing very similar behaviour with respect to the 1.0 - 1.4 interval). We considered both the BC03- and the CB07-based observed GSMF. Despite the different physical recipes adopted by the different semi-analytical models, their predictions are remarkably similar (as already found by Fontanot et al. 2009). All the models considered consistently predict a larger abundance of low mass galaxies with respect to observations at least up to  $z \sim 3$ , despite the steep low-mass-end slope inferred with our data. The only exception is the Wang et al. (2008) model, which is closer to the observations at  $z \sim 2.2$  and consistent with them at  $z \sim 3$ . The general overestimation of the faint-end is due to the documented too efficient formation of low-to-intermediate mass ( $10^9 - 10^{11} M_\odot$ ) galaxies in the models (Fontanot et al. 2009, see also Lo Faro et al. 2009) and it is not explained by systematic uncertainties due to the stellar templates. On the observational side, it is unlikely that so many low mass galaxies are missed by the data, especially at low redshift ( $z \sim 1$ ), when the disagreement is already in place for  $M_* > 10^{10} M_\odot$ . In our highest redshift bin ( $3.5 < z < 4.5$ ) MORGANA, the Wang et al. (2008) and the Somerville et al. (2011) models show a reasonable agreement with the data, while the Menci et al. (2006) model still slightly overpredicts the space density of low mass galaxies. This is due to the fact that the latter includes starburst events triggered by fly-by interactions, which are very common in low mass objects at high redshift and increase their the stellar mass. All theoretical predictions also underestimate the stellar mass of high mass galaxies in the highest redshift bin. However, this mass range is highly affected by cosmic variance, and the low ( $\leq 3$ ) number of galaxies observed with our data in each of the highest mass bins ( $M > 10^{11} M_\odot$ ) prevents firm conclusions. It is worth mentioning that Marchesini et al. (2009) found a similar disagreement at high masses, using observations on a sky area  $\sim 10$  times larger than the area sampled by this study.

A different treatment for the TP-AGB phase in the stellar population synthesis models (i.e. moving from BC03 to CB07) may indeed help in reducing the high-mass end discrepancy, by reducing the inferred stellar masses of the galaxies in the sample. As a matter of fact, Henriques et al. (2011) demonstrated that the inclusion of a more detailed treatment of the TP-AGB phase in the semi-analytical framework solves a comparable mismatch between the predicted and observed rest-frame  $K$  band luminosity function of bright galaxies at  $z \sim 2 - 3$ , by increasing the

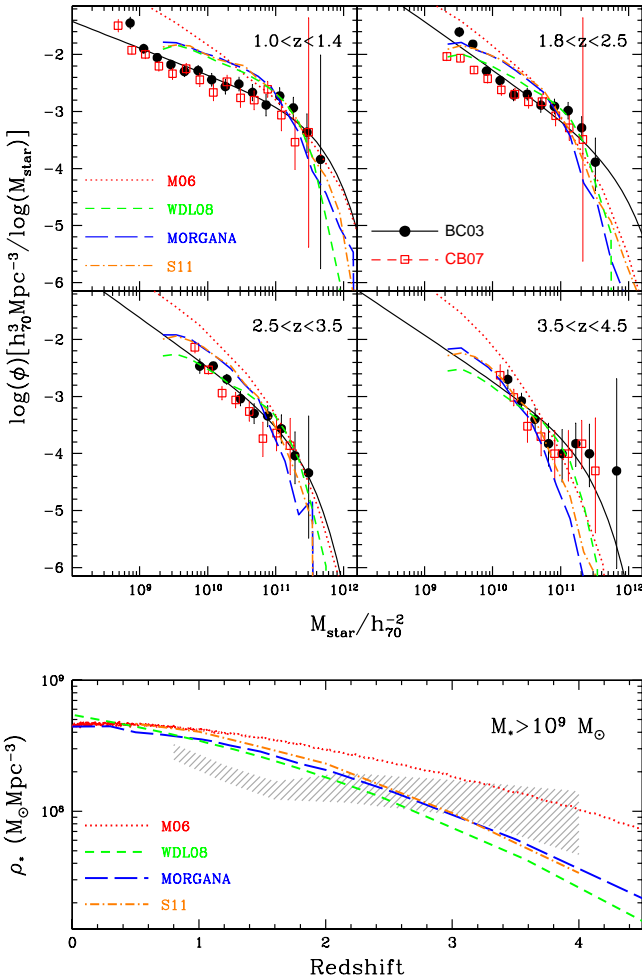


**Fig. 10.** Observed stellar mass functions in different redshift ranges (upper) and observed stellar mass density between  $10^9$  and  $10^{13} M_\odot$  (lower) compared with theoretical predictions, shown as coloured curves. Red dotted curves: Menci et al. (2006). Blue long-dashed curves: MORGANA (Monaco et al. 2007). Green dashed curves: Wang et al. (2008). Orange dot-dashed curves: Somerville et al. (2011). Black solid circles, solid lines, red open boxes and the gray shaded area show the results of the present work as in Figs. 5 and 9.

predicted  $K$ -band flux in model galaxies. This effect is particularly relevant at these cosmic ages, since model galaxies are dominated by intermediate age stellar populations, with the right age ( $\sim 1$  Gyr) to develop a TP-AGB phase which makes them redder without the need of changing their mass or age. We test this idea by considering stellar masses estimated using the CB07 synthetic templates. However, as clearly shown in Fig. 10 (upper panel, red open boxes), assuming stellar templates which account for TP-AGB stars alleviates (the number of  $M > 10^{11} M_\odot$  galaxies in the sample is reduced by 37%) but does not completely solve the mismatch at the high-mass-end of the GSMF in the highest redshift bin (where the previous percentage reduces to 12.5%).

We also compared the SMD locked in  $10^9 < M_*/M_\odot < 10^{13}$  galaxies, as predicted by the four models we consider (lower panel of Fig. 10), and we found that it is on average larger than what observed by a factor of  $\sim 2$  up to  $z \sim 2$ . MORGANA, the

Wang et al. (2008) and the Somerville et al. (2011) models show a good agreement with our results at  $2 \leq z \leq 3$ , and are below the data at the highest redshifts. Menci et al. (2006) prediction, given its overall steeper low-mass-end, is instead larger than the observed SMD up to  $z \sim 3$ . These results are driven by the already mentioned overabundance of intermediate-to-low-mass galaxies, which dominate the SMD at all redshifts, and counterbalanced by the overestimation of the stellar mass in massive galaxies at high redshift.

## 7. Summary

We used deep near-IR observations ( $Y$  down to 27.3,  $J$  and  $H$  down to 27.4 AB mag at  $5\sigma$ ) carried out with the Wide Field Camera 3 in the GOODS-S field as part of the Early Release Science. These, complemented with the deep  $K_S$  (down to 25.5 at  $5\sigma$ ) Hawk-I band and with high quality photometry in various bands from the near-UV to  $8 \mu\text{m}$ , were used to derive accurate estimates of the stellar mass. The average relative error on the stellar mass for a given object has decreased by  $\sim 30\%$  with respect to what obtained with the GOODS-MUSIC catalog in previous works from our group.

Unfortunately, the sky region covered by ERS observations is biased by a number of localized as well as diffuse overdensities (Vanzella et al. 2005; Castellano et al. 2007; Salimbeni et al. 2009a; Yang et al. 2010), which could be responsible for oscillations in the normalization of the GSMF given the limited size of the area. However, this data set offers a unique combination of accuracy in photometric quality (and hence in photometric redshifts and stellar mass) and depth, which makes it ideally suited to study the faint-end of the stellar mass function.

We computed the stellar mass functions in 6 different redshift intervals between 0.6 and 4.5. Thanks to the depth of the catalog, we were able to push the low-mass-end sampling at fainter values with respect to most previous studies by 0.5 dex up to  $z \sim 1.8$  and 0.1 dex at  $z \sim 4$ . We compared our results with previous works and we found general good agreement, even at the highest masses despite the limited sky area sampled by our data set. The only redshift intervals which show a poorer agreement with previous results are those between  $z = 1.4$  and  $z = 2.5$ , which are known to be affected by the presence of overdensities: we find, as expected, a slightly larger abundance of massive galaxies. We also compared the GSMF obtained with two different stellar libraries: BC03 templates and CB07 ones, the latter including a treatment of TP-AGB stars. The stellar masses inferred from the CB07 library are on average 0.12 dex lower than the BC03-based ones, with a large (0.17 dex) scatter. The lack of a clear trend with stellar mass or redshift of the ratio between the two estimates translates into a lack of systematic difference between the best fit Schechter parameters in the two cases. The largest disagreement was found at  $z \sim 2 - 3$ , where the effect of the TP-AGB phase is expected to be most important.

The main result of this study is the steepening of the faint-end slope: the value of  $\alpha$  increases from  $-1.44 \pm 0.03$  at  $z \sim 0.8$  to  $-1.86 \pm 0.16$  at  $z \sim 3$ , and it flattens up to  $z \sim 4$ . The steepening of the low-mass-end, already pointed out by previous authors, is here confirmed with deeper and higher quality photometry. Our results are not affected by degeneracies of the  $M^*$  parameter, and they are solid against the choice of the stellar templates and of the functional shape fitted to the GSMF, as well as against the limitations derived from the small area covered by ERS observations.

We computed the stellar mass density as a function of redshift and compared it with the integrated star formation history

of Hopkins & Beacom (2006) and Reddy & Steidel (2009). The better sampling of the GSMF at low masses and the steep faint-end slopes inferred determine higher SMD estimates at  $z > 2$  compared to most previous works, solving the disagreement observed by previous authors between the SMD and the integrated SFRD at these redshifts. However, despite the steep GSMF that we find, the integrated star formation history still exceeds the direct measure of the stellar mass density at  $z \sim 2$  by a factor of  $\sim 2 - 3$ , even when our data are analysed together with the results of previous large surveys in order to achieve a good sampling also of the bright-end tail of the GSMF.

Finally, we compared our GSMF and SMD estimates with the predictions of four models of galaxy formation and evolution. All models predict a larger abundance of low mass galaxies with respect to observations, at least up to  $z \sim 3$ . They also underestimate the stellar mass of high mass galaxies in the highest redshift bin, although cosmic variance effects prevent us from drawing firm conclusions at these redshifts. The overabundance of low mass galaxies translates into a general overestimation of the total stellar mass density with respect to the data up to  $z \sim 2$ , while the latter is underestimated at  $z \gtrsim 3$  due to the dearth of massive galaxies at these redshifts. The exact degree of disagreement depends on the different model.

Future CANDELS data will be covering a larger sky area and will allow a better sampling of the bright-end of the GSMF and of its normalization, and at the same time they will be deep enough to accurately probe its faint-end. These, together with spectroscopic follow-up campaigns, will reduce the uncertainties on the stellar masses, and they will significantly improve our results and our understanding of the stellar mass assembly process.

**Acknowledgements.** The authors thank M. Bolzonella, O. Ilbert, M. Kajisawa, L. Pozzetti for providing their estimates of the mass function, and N. Reddy for supplying the functional shape used to fit the SFRD. This work is based on observations made with the NASA/ESA Hubble Space Telescope, obtained from the data archive at the Space Telescope Institute. STScI is operated by the association of Universities for Research in Astronomy, Inc. under the NASA contract NAS 5-26555. Observations were also carried out using the Very Large Telescope at the ESO Paranal Observatory under Programme IDs LP181.A-0717, ID 170.A-0788, and the ESO Science Archive under Programme IDs 67.A-0249, 71.A-0584, 69.A-0539. We acknowledge financial contribution from the agreement ASI-INAF I/009/10/0".

## References

Alonso-Herrero, A., Pérez-González, P. G., Rieke, G. H., et al. 2008, *ApJ*, 677, 127

Bolzonella, M., Kovač, K., Pozzetti, L., et al. 2010, *A&A*, 524, A76+

Brusa, M., Fiore, F., Santini, P., et al. 2009, *A&A*, 507, 1277

Bruzual, G. 2007, in *Astronomical Society of the Pacific Conference Series*, Vol. 374, From Stars to Galaxies: Building the Pieces to Build Up the Universe, ed. A. Vallenari, R. Tantalo, L. Portinari, & A. Moretti, 303–+

Bruzual, G. & Charlot, S. 2003, *Royal Astronomical Society, Monthly Notices*, 344, 1000

Bundy, K., Georgakakis, A., Nandra, K., et al. 2008, *ApJ*, 681, 931

Caputi, K. I., Cirasuolo, M., Dunlop, J. S., et al. 2011, *MNRAS*, 413, 162

Castellano, M., Fontana, A., Boutsia, K., et al. 2010a, *A&A*, 511, A20+

Castellano, M., Fontana, A., Paris, D., et al. 2010b, *A&A*, 524, A28+

Castellano, M., Salimbeni, S., Trevese, D., et al. 2007, *ApJ*, 671, 1497

Cole, S., Aragon-Salamanca, A., Frenk, C. S., Navarro, J. F., & Zepf, S. E. 1994, *MNRAS*, 271, 781

Daddi, E., Cimatti, A., Renzini, A., et al. 2004, *ApJ*, 617, 746

De Santis, C., Grazian, A., Fontana, A., & Santini, P. 2007, *New Astronomy*, 12, 271

Dickinson, M., Papovich, C., Ferguson, H. C., & Budavári, T. 2003, *ApJ*, 587, 25

Drory, N. & Alvarez, M. 2008, *ApJ*, 680, 41

Drory, N., Bender, R., Feulner, G., et al. 2004, *The Astrophysical Journal*, 608, 742

Drory, N., Bundy, K., Leauthaud, A., et al. 2009, *ApJ*, 707, 1595

Drory, N., Salvato, M., Gabasch, A., et al. 2005, *ApJ*, 619, L131

Fardal, M. A., Katz, N., Weinberg, D. H., & Davé, R. 2007, *MNRAS*, 379, 985

Fioc, M. & Rocca-Volmerange, B. 1997, *A&A*, 326, 950

Fontana, A., Donnarumma, I., Vanzella, E., et al. 2003, *The Astrophysical Journal Letters*, 594, L9

Fontana, A., Pozzetti, L., Donnarumma, I., et al. 2004, *Astronomy & Astrophysics*, 424, 23

Fontana, A., Salimbeni, S., Grazian, A., et al. 2006, *A&A*, 459, 745

Fontanot, F., De Lucia, G., Monaco, P., Somerville, R. S., & Santini, P. 2009, *MNRAS*, 397, 1776

Giallongo, E., D'Odorico, S., Fontana, A., et al. 1998, *AJ*, 115, 2169

Giavalisco, M., Ferguson, H. C., Koekemoer, A. M., et al. 2004, *ApJ*, 600, L93

González, V., Labbé, I., Bouwens, R. J., et al. 2011, *ApJ*, 735, L34+

Grazian, A., Castellano, M., Koekemoer, A. M., et al. 2011, *A&A*, 532, A33+

Grazian, A., Fontana, A., De Santis, C., et al. 2006, *Astronomy & Astrophysics*, 449, 951

Grogan, N. A., Kocevski, D. D., Faber, S. M., et al. 2011, *ApJS*, in press, arXiv: 1105.3753

Henriques, B., Maraston, C., Monaco, P., et al. 2011, *MNRAS*, 415, 3571

Hopkins, A. M. & Beacom, J. F. 2006, *ApJ*, 651, 142

Ilbert, O., Salvato, M., Le Floc'h, E., et al. 2010, *ApJ*, 709, 644

Kajisawa, M., Ichikawa, T., Tanaka, I., et al. 2009, *ApJ*, 702, 1393

Koekemoer, A. M., Faber, S. M., Ferguson, H. C., et al. 2011, *ApJS*, in press, arXiv: 1105.3754

Lee, S.-K., Ferguson, H. C., Somerville, R. S., Wiklind, T., & Giavalisco, M. 2010, *ApJ*, 725, 1644

Lo Faro, B., Monaco, P., Vanzella, E., et al. 2009, *MNRAS*, 399, 827

Magliocchetti, M., Santini, P., Rodighiero, G., et al. 2011, *MNRAS*, 416, 1105

Maiolino, R., Nagao, T., Grazian, A., et al. 2008, *A&A*, 488, 463

Maraston, C. 2005, *MNRAS*, 362, 799

Maraston, C., Pforr, J., Renzini, A., et al. 2010, *MNRAS*, 407, 830

Marchesini, D. & van Dokkum, P. G. 2007, *ApJ*, 663, L89

Marchesini, D., van Dokkum, P. G., Förster Schreiber, N. M., et al. 2009, *ApJ*, 701, 1765

Marchesini, D., Whitaker, K. E., Brammer, G., et al. 2010, *ApJ*, 725, 1277

Marigo, P., Girardi, L., Bressan, A., et al. 2008, *A&A*, 482, 883

Menci, N., Fontana, A., Giallongo, E., Grazian, A., & Salimbeni, S. 2006, *The Astrophysical Journal*, 647, 753

Monaco, P., Fontanot, F., & Taffoni, G. 2007, *MNRAS*, 375, 1189

Mortlock, A., Conselice, C. J., Bluck, A. F. L., et al. 2011, *MNRAS*, 413, 2845

Nonino, M., Dickinson, M., Rosati, P., et al. 2009, *ApJS*, 183, 244

Nordon, R., Lutz, D., Shao, L., et al. 2010, *A&A*, 518, L24+

Papovich, C., Finkelstein, S. L., Ferguson, H. C., Lotz, J. M., & Giavalisco, M. 2011, *MNRAS*, 412, 1123

Pérez-González, P. G., Rieke, G. H., Villar, V., et al. 2008, *ApJ*, 675, 234

Poli, F., Menci, N., Giallongo, E., et al. 2001, *ApJ*, 551, L45

Pozzetti, L., Bolzonella, M., Lamareille, F., et al. 2007, *A&A*, 474, 443

Pozzetti, L., Bolzonella, M., Zucca, E., et al. 2010, *A&A*, 523, A13+

Reddy, N. A. & Steidel, C. C. 2009, *ApJ*, 692, 778

Reed, D. S., Bower, R., Frenk, C. S., Jenkins, A., & Theuns, T. 2007, *MNRAS*, 374, 2

Rodighiero, G., Cimatti, A., Gruppioni, C., et al. 2010, *A&A*, 518, L25+

Rudnick, G., Rix, H., Franx, M., et al. 2003, *ApJ*, 599, 847

Salimbeni, S., Castellano, M., Pentericci, L., et al. 2009a, *A&A*, 501, 865

Salimbeni, S., Fontana, A., Giallongo, E., et al. 2009b, in *American Institute of Physics Conference Series*, Vol. 1111, *American Institute of Physics Conference Series*, ed. G. Giobbi, A. Tornambe, G. Raimondo, M. Limongi, L. A. Antonelli, N. Menci, & E. Brocato, 207–211

Sandage, A., Tammann, G. A., & Yahil, A. 1979, *ApJ*, 232, 352

Santini, P., Fontana, A., Grazian, A., et al. 2009, *A&A*, 504, 751

Santini, P., Rosario, D., Shao, L., et al. 2011, *A&A*, submitted

Schmidt, M. 1968, *ApJ*, 151, 393

Silverman, J. D., Lamareille, F., Maier, C., et al. 2009, *ApJ*, 696, 396

Somerville, R. S., Gilmore, R. C., Primack, J. R., & Dominguez, A. 2011, *MNRAS*, submitted, arXiv: 1104.0669

Vanzella, E., Cristiani, S., Dickinson, M., et al. 2005, *A&A*, 434, 53

Wang, J., De Lucia, G., Kitzbichler, M. G., & White, S. D. M. 2008, *MNRAS*, 384, 1301

Wilkins, S. M., Trentham, N., & Hopkins, A. M. 2008, *MNRAS*, 385, 687

Windhorst, R. A., Cohen, S. H., Hathi, N. P., et al. 2011, *ApJS*, 193, 27

Xue, Y. Q., Brandt, W. N., Luo, B., et al. 2010, *ApJ*, 720, 368

Yang, Y., Zabludoff, A., Eisenstein, D., & Davé, R. 2010, *ApJ*, 719, 1654